Stimulated rotational Raman scattering of arbitrarily polarized broadband light

R. H. Lehmberg,[1,*] M. F. Wolford,[2] J. L. Weaver,[2] D. Kehne,[2] S. P. Obenschain,[2] D. Eimerl,[3,†] and J. P. Palastro[4]

[1]*Consultant to Naval Research Laboratory through RSI Corporation, Lanham, Maryland 20706, USA*

[2]*Plasma Physics Division, Naval Research Laboratory, Washington, DC 20375, USA*

[3]*Eimex Software and Consulting, Inc., Fairfield, California 94534, USA*

[4]*Laboratory for Laser Energetics, University of Rochester, Rochester, New York 14623, USA*

(Received 12 August 2020; accepted 18 November 2020; published 23 December 2020)

Laser plasma instabilities are problematic for inertial confinement fusion because they can spoil illumination uniformity, reduce laser-target coupling, and create unwanted fast electrons. Recent experiments and simulations have shown that self-seeded stimulated rotational Raman scattering (SRRS) in air might achieve enough spectral broadening to mitigate these instabilities with only moderate unwanted broadening of the focal spot. The theoretical model for the simulations included chaotic broadband and spatially multimode light, but was a scalar formulation suitable for only linear polarization, where the SRRS gains and spectral broadening are limited by Stokes–anti-Stokes coupling. This paper derives a tensor formulation of SRRS theory suitable for modeling spectral broadening of arbitrarily polarized spatially and temporally incoherent light; it then describes the algorithms used to simulate the theory and provides some preliminary results that compare linear and elliptical polarizations. It begins with a paraxial wave equation for an arbitrarily polarized optical field envelope, which is phase modulated by a term proportional to a Raman driven molecular polarizability tensor. Treating the air molecules as rigid rotators, it uses a quantum treatment to derive a driven harmonic oscillator equation for that polarizability, then expresses these vector and tensor equations in terms of the field's right- and left-handed circular polarization components to derive the final coupled equations for arbitrary polarization. The formulation includes possible ac Stark shift contributions, but shows that they are negligible for intensities below $10\,\mathrm{GW/cm^2}$. It then describes the algorithms used in the simulation code and the numerical model of the chaotic light, whose initial spectral bandwidth is broad enough to self-seed the SRRS. In this algorithm, the SRRS process accurately conserves the total energy at each axial plane along the propagation path. Finally, it compares simulations of power spectra and far-field profiles for elliptical vs linear polarization, which show that elliptically polarized light produces significantly more broadening of both profiles than linear polarization. For linear polarization, the SRRS process reduces the incident coherence time from 0.54 to 0.27 ps; for elliptical polarization, it reduces to 0.19 ps. The theory and simulation algorithms presented here provide a framework for evaluating techniques that combine beams of alternating circular polarizations with different spectra and angular divergences to improve SRRS spectral broadening without excessive focal spot broadening.

DOI: 10.1103/PhysRevA.102.063530

I. INTRODUCTION

Large optical bandwidths have been predicted for some time to mitigate the laser-plasma instability (LPI) that can spoil illumination uniformity, reduce laser-target coupling, and create unwanted fast electrons in inertial confinement fusion (ICF) experiments [1]. LPI occurs mainly in the corona plasma at near or below quarter critical densities and includes the cross-beam energy transfer (CBET) instability [2] driven by stimulated Brillouin scattering, plus the two-plasmon decay (TPD) and stimulated Raman scattering (SRS) instabilities [3] driven by Langmuir waves. Recent simulations suggest that ≈8 THz, which is equivalent to ≈0.125-ps coherence time, is required to quench the CBET instability [4], while earlier simulations estimate similar requirements for TPD [5] and SRS [6].

These bandwidths are well beyond the intrinsic capabilities of current ICF drivers [7], with the possible exception of the 193-nm argon fluoride excimer laser [8], which is still under development. One must therefore examine the spectral broadening capabilities of nonlinear optical processes, such as stimulated rotational Raman scattering (SRRS) [9,10], self-phase modulation (SPM) [11], or parametric amplification [12] in the propagation paths between the laser and focusing optics. Efficient SPM is possible for krypton fluoride (KrF) light in xenon because of a large negative nonlinear refractive index enhanced by a two-photon near-resonance at 248 nm. This has the added advantage of removing self-focusing issues, but the effective spectral width is likely to be limited to <6 THz by the 11.9-THz detuning of the two-photon resonance. Parametric amplification may allow bandwidths up to 10 THz from 351-nm glass systems, but is still under early development. This paper will concentrate on the SRRS approach.

*robert.lehmberg.ctr@nrl.navy.mil

†Deceased.

SRRS occurs naturally when the laser output beams excite rotational quantum states of air molecules along their propagation paths to the target chamber [13,14], resulting in the generation of Stokes and anti-Stokes sidebands in the spectra and possible degradation of the beam quality. With sufficient uncontrolled growth, this process can spoil an implosion by broadening the final focal profile, and reducing the focusable drive energy that impacts the target [15–17]. It can grow from ambient fluctuations or can be seeded by laser light either from within the spectrum of a broadband primary beam or from a copropagating secondary beam. Its growth rate depends on the composition of the transport media, the path length, the intensity, and the coherence properties of the beam [18–21]. SRRS is normally regarded as detrimental to ICF laser systems and is suppressed on very large lasers such as the National Ignition Facility by using tubes filled with an atomic gas (such as argon) to transport the beams to the target chamber [22].

Reference [10] reported new experimental and theoretical results on the Nike KrF laser suggesting that properly seeded SRRS can significantly broaden the spectral bandwidth without excessive broadening of the focal spot. Specifically we reported spectral broadening by SRRS generated in the long air paths required for Nike's angularly multiplexed beams [23]. While SRRS is not a constraint on normal Nike operation due to the low beam intensities, significant SRRS was generated by lengthening the air paths and using shorter higher intensity pulses. It can be a self-seeded process if the spectrum of the primary beam is sufficiently broad or it can be seeded by weaker copropagating beams.

Nike uses a beam smoothing technique called echelon-free induced spatial incoherence (ISI), which produces a focal spot with a time-averaged uniformity within 1% and a typical diameter of $\approx 100\times$ diffraction limit (XDL) [24–27]. This spot size results from the $\Delta\theta_{\mathrm{ISI}} \sim 100$ XDL angular divergence of the spatially incoherent light in the laser's near field, so it should remain relatively insensitive to additional divergence from SRRS as long as it remains much smaller than $\Delta\theta_{\mathrm{ISI}}$. In our recent experiments, which used $\approx 25-30$ XDL beams, the measured and simulated focal profiles for beams experiencing significant SRRS growth were found to have moderate changes, mainly in their outer skirts [10].

So far, Nike experiments have used only linearly polarized light, which we have adequately modeled by a scalar paraxial wave equation for the optical field and a scalar driven harmonic oscillator equation for the Raman excitation [10]. The main limitation of this is a parametric SRRS gain suppression mechanism that has been observed by earlier authors [28–30] with linearly polarized light in gases. Linear polarization allows a Raman Stokes–anti-Stokes (SAS) coupling term that creates a parasitic redistribution of Stokes energy into the anti-Stokes wave; this allows both waves to grow together linearly, but not exponentially. Normal exponential Stokes growth is achieved only when the divergence angle between the Stokes and anti-Stokes waves is large enough to introduce a phase mismatch that suppresses the SAS coupling. The efficiency of SRRS spectral broadening is therefore largest for those wave pairs likely to contribute the most to focal spot broadening.

To avoid this issue and increase flexibility, we have generalized the SRRS theory to a full tensor formulation that allows light of arbitrary polarization. Although the simulations shown here model only the Nike laser, this formulation can also model glass lasers with spatially coherent input beams [9,12], where filamentation may be an issue. (The SRRS gain coefficient and nonlinear refractive index are somewhat lower at 351 nm, so one could use higher intensities.) Following earlier work by Palastro [31] on self-phase modulation of ultrashort pulses in air, we derive the full tensor working equations for the SRRS excitation directly from the molecular rigid rotator (RR) model. These results can also be derived from a quasi-three-level (Q3L) Raman model based on a generalization of Penano's scalar formulation [32], but the intermediate states make the derivation more complicated [33,34]. The two approaches complement one another; the Q3L model emphasizes the quantum nature of the Raman process and would be required if any intermediate state is nearly resonant with the light [35], while the RR model is more intuitive, introduces the key polarizability anisotropy parameter at the outset, and avoids dealing with the intermediate states of the Q3L model.

In Sec. II, we apply the RR model to derive a pair of coupled vector and tensor equations for an arbitrarily polarized optical amplitude $\mathbf{E}$ phase-modulated by a Raman-driven molecular polarizability tensor $\langle\boldsymbol{\alpha}\rangle$. We then expand these equations explicitly in terms of the right- and left-handed circular polarization components of $\mathbf{E}$ and related components of $\langle\boldsymbol{\alpha}\rangle$. This formulation includes ac Stark shift contributions, but concludes that they are negligible under conditions of interest here. Section III describes the algorithms used in the simulation code and the numerical model of the incident ISI light. This algorithm accurately conserves the total energy at each axial plane along the propagation path. Section IV compares SRRS simulations with linear and elliptical incident polarization, showing that elliptical polarization produces significantly more broadening of both spectral and far-field profiles than linear polarization. Section V confirms that the ac Stark shifts are much smaller than the pressure-broadened Raman linewidths at intensities below 10 GW/cm^2, while Sec. VI summarizes our results and proposes future work.

II. COUPLED SRRS EQUATIONS

A. Paraxial wave equation and RR molecular model

The formulation begins with the full electromagnetic wave equation for the total optical field $\mathbb{E}$ driven by a nonlinear polarization $\mathbb{P}^{\mathrm{SRS}}$ whose frequency sidebands include numerous $\approx$ THz rotational Raman transitions in N_2 and O_2. Unlike the usual treatments of Raman scattering [36,37], this formulation envelopes $\mathbb{E}$ and $\mathbb{P}^{\mathrm{SRS}}$ to only a single temporal-spatial carrier frequency $\omega_0 = 2\pi c/\lambda_0$ and $k_0 = n_0\omega_0/c$ located at the respective centers of the incident temporal and spatial spectra, as follows:

$$\mathbb{E}(\mathbf{x},t) = \mathrm{Re}[\mathbf{E}(\mathbf{x},t)\exp(ik_0 z - i\omega_0 t)],$$

$$\mathbb{P}_{\mathrm{SRS}}(\mathbf{x},t) = \mathrm{Re}[\mathbf{P}_{\mathrm{SRS}}(\mathbf{x},t)\exp(ik_0 z - i\omega_0 t)].$$

Here $\mathbf{x} \equiv (\mathbf{x}_\perp, z)$, z is the axial propagation distance, $\mathbf{x}_\perp \equiv (x,y)$ are the transverse coordinates, and $\mathbf{E}(\mathbf{x},t)$ and $\mathbf{P}_{\mathrm{SRS}}(\mathbf{x},t)$ are transverse-polarized slowly-varying complex amplitudes. These amplitudes carry all

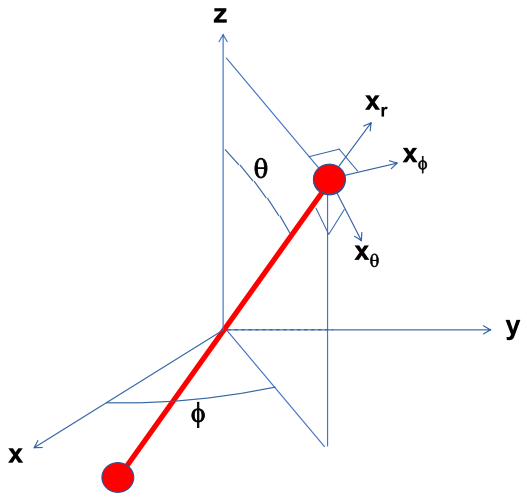

FIG. 1. Spherical coordinate system with molecular axis along $\hat{\mathbf{r}}$ and $\mathbf{k_0}$ along $\hat{\mathbf{z}}$.

the information about the Raman processes, so the Stokes and anti-Stokes shifts appear, respectively, as equal negative and positive frequency components. Because we are dealing with rotational transitions and paraxial conditions, the spatial and spectral bandwidths remain negligible compared to the carrier frequencies. Substituting these expansions into the wave equation and applying the paraxial and slowly varying envelope approximations, we obtain [32]

$$\left(\partial_z + \frac{1}{2ik_0}\nabla_\perp^2 + i\frac{1}{2}\beta\partial_\tau^2\right)\mathbf{E} = i\frac{\omega_0}{2n_0c}4\pi\mathbf{P}_{\rm SRS} + ik_0n_2^I|\mathbf{E}|^2\mathbf{E}, \tag{1}$$

where $\nabla_\perp^2 \equiv \partial_x^2 + \partial_y^2$, $\tau \equiv t - z/v_g = t - z(\partial_\omega k)_0$ is the retarded time, $\beta = (\partial_\omega^2 k)_0$ is the group velocity dispersion (GVD), n_2^I is the near-instantaneous electronic part of the nonlinear refractive index [38], $\mathbf{P}_{\rm SRS}(\mathbf{x},\tau) = N\langle\mathbf{p}_{\rm SRS}(\mathbf{x},\tau)\rangle$ is the nonlinear polarization found by ensemble averaging the SRRS-induced molecular dipole moment amplitudes $\mathbf{p}_{\rm SRS}(\mathbf{x},\tau)$ over all orientations, and N is the molecular density. For brevity, we will display $(\mathbf{x},\tau)$ labels only if needed for clarity and temporarily set aside the $n_2^I|\mathbf{E}|^2$ terms to focus on $\mathbf{P}_{\rm SRS}$.

The treatment of $\mathbf{P}_{\rm SRS}$ is based on Palastro's rigid rotator model [31], but extends the analysis to the full SRRS case where each $j \to j+2$ rotational transition has a well-defined linewidth. It also uses the conventional spherical coordinate system shown in Fig. 1, where the polar axis $\hat{\mathbf{z}}$ lies along the laser propagation direction $\hat{\mathbf{k}}_0$, rather than one polarization direction. This simplifies the derivation and leads directly to the spherical harmonic rotational wave functions; it also allows a simple derivation of the ac Stark shift terms [39–41], which can be an issue at intensities significantly above $10\,\mathrm{GW/cm^2}$.

In Fig. 1, the molecular axis $\hat{\mathbf{x}}_\parallel \equiv \hat{\mathbf{r}}$ lies along the polar angle θ, so the orthogonal axes are $\hat{\mathbf{x}}_{\perp 1} \equiv \hat{\theta}$ and $\hat{\mathbf{x}}_{\perp 2} \equiv \hat{\phi}$. From the axial $\alpha_\parallel$ and transverse $\alpha_\perp$ polarizabilities and the identity $\hat{\mathbf{r}}\hat{\mathbf{r}} + \hat{\boldsymbol{\theta}}\hat{\boldsymbol{\theta}} + \hat{\boldsymbol{\phi}}\hat{\boldsymbol{\phi}} = \bar{\mathbf{I}}$, we write the *total* induced polarization $\mathbf{P}_{\rm tot} = N\langle\mathbf{p}_{\rm tot}\rangle$ in the general form

$$\begin{aligned}\mathbf{P}_{\rm tot}/N &= \langle\alpha_\parallel\hat{\mathbf{r}}\hat{\mathbf{r}} + \alpha_\perp\hat{\boldsymbol{\theta}}\hat{\boldsymbol{\theta}} + \alpha_\perp\hat{\boldsymbol{\phi}}\hat{\boldsymbol{\phi}}\rangle\cdot\mathbf{E}\\ &= \alpha_\perp\mathbf{E} + \Delta\alpha\langle\hat{\mathbf{r}}\hat{\mathbf{r}}\rangle\cdot\mathbf{E},\end{aligned} \tag{2}$$

where the $\langle\rangle$ brackets denote an ensemble average over all molecular orientations and $\Delta\alpha \equiv \alpha_\parallel - \alpha_\perp$ is the polarizability anisotropy. The first term accounts for $\approx 2/3$ of the linear refraction, while the second accounts for both linear and SRRS contributions. To separate these, we rewrite the dyadic variable $\hat{\mathbf{r}}\hat{\mathbf{r}}$ as $\hat{\mathbf{r}}\hat{\mathbf{r}} = \hat{\mathbf{r}}^0\hat{\mathbf{r}}^0 + (\hat{\mathbf{r}}\hat{\mathbf{r}} - \hat{\mathbf{r}}^0\hat{\mathbf{r}}^0)$, where $\hat{\mathbf{r}}^0\hat{\mathbf{r}}^0$ is the zeroth-order linear term with the Cartesian components

$$\begin{bmatrix}\sin^2\theta\cos^2\phi & \sin^2\theta\cos\phi\sin\phi & \sin\theta\cos\theta\cos\phi\\ \sin^2\theta\sin\phi\cos\phi & \sin^2\theta\sin^2\phi & \sin\theta\cos\theta\sin\phi\\ \cos\theta\sin\theta\cos\phi & \cos\theta\sin\theta\sin\phi & \cos^2\theta\end{bmatrix},$$

which immediately give the ensemble-average value

$$\langle\hat{\mathbf{r}}^0\hat{\mathbf{r}}^0\rangle = \frac{1}{4\pi}\oint\hat{\mathbf{r}}^0\hat{\mathbf{r}}^0 d\Omega = \frac{1}{3}\bar{\mathbf{I}}.$$

The total induced polarization $\mathbf{P}_{\rm tot} = \mathbf{P}_{\rm lin} + \mathbf{P}_{\rm SRS}$ follows from (2) and

$$\begin{aligned}\mathbf{P}_{\rm lin}(\mathbf{x},\tau) &= \chi_{\rm lin}\mathbf{E}(\mathbf{x},\tau),\\ \mathbf{P}_{\rm SRS}(\mathbf{x},\tau) &= \bar{\boldsymbol{\chi}}(\mathbf{x},\tau)\cdot\mathbf{E}(\mathbf{x},\tau),\end{aligned}$$

where the respective linear and SRRS susceptibilities are

$$\chi_{\rm lin} = N\alpha_{\rm lin} = N\left(\tfrac{2}{3}\alpha_\perp + \tfrac{1}{3}\alpha_\parallel\right), \tag{3a}$$

$$\begin{aligned}\bar{\boldsymbol{\chi}}(\mathbf{x},\tau) &= N\langle\boldsymbol{\alpha}(\mathbf{x},\tau)\rangle\\ &= N\Delta\alpha\langle\hat{\mathbf{r}}\hat{\mathbf{r}} - \hat{\mathbf{r}}^0\hat{\mathbf{r}}^0\rangle = N\Delta\alpha\left(\langle\hat{\mathbf{r}}\hat{\mathbf{r}}\rangle - \tfrac{1}{3}\bar{\mathbf{I}}\right),\end{aligned} \tag{3b}$$

and the SRRS molecular polarizability tensor has the quadrupole form

$$\boldsymbol{\alpha}(\mathbf{x},\tau) \equiv \Delta\alpha(\hat{\mathbf{r}}\hat{\mathbf{r}} - \hat{\mathbf{r}}^0\hat{\mathbf{r}}^0) \to \Delta\alpha\left(\hat{\mathbf{r}}\hat{\mathbf{r}} - \tfrac{1}{3}\bar{\mathbf{I}}\right). \tag{4}$$

The linear susceptibility $N\alpha_{\rm lin}$, which initially appeared on the right-hand side of the full wave equation, has been incorporated into $n_0(\omega_0) = 1 + 2\pi\chi_{\rm lin}$ and the factors v_g and β on the left-hand side of Eq. (1); hence $\mathbf{P}_{\rm SRS} = \bar{\boldsymbol{\chi}}\cdot\mathbf{E} = N\langle\boldsymbol{\alpha}\rangle\cdot\mathbf{E}$ and Eq. (1) becomes

$$\left(\partial_z + \frac{1}{2ik_0}\nabla_\perp^2 + i\frac{1}{2}\beta\partial_\tau^2\right)\mathbf{E} = i2\pi\frac{\omega_0}{n_0c}N\langle\boldsymbol{\alpha}\rangle\cdot\mathbf{E}. \tag{5}$$

B. Quantum treatment of RR molecular Raman response

To treat the polarizability tensor (4) quantum mechanically, we define $\boldsymbol{\alpha} = \Delta\alpha(\hat{\mathbf{r}}\hat{\mathbf{r}} - \frac{1}{3}\bar{\mathbf{I}})$ as a quadrupole operator and for simplicity restrict the wave function $|\psi(\mathbf{x},\tau)\rangle$ to comprise only one pair of degenerate molecular rotational levels $|j,m\rangle$ and $|J,M\rangle$, with $J = j+2$, as allowed by the quadrupole selection rules; the corresponding energy difference is then $\hbar\omega_j = hcB(4j+6)$ [42]. This restriction will be lifted near

the end of the derivation by summing the results over all thermally occupied rotational level pairs of the N_2 and O_2 components of air. The ensemble averaged polarizability $\langle\boldsymbol{\alpha}\rangle$ in Eq. (4) thus temporarily reduces to

$$\begin{aligned}\langle\boldsymbol{\alpha}\rangle_j &= \langle\langle\psi((\mathbf{x},\tau))|\boldsymbol{\alpha}|\psi((\mathbf{x},\tau))\rangle\rangle \\ &= \Delta\alpha\big[\langle\langle\psi(\mathbf{x},\tau)|\hat{\mathbf{r}}\hat{\mathbf{r}}|\psi(\mathbf{x},\tau)\rangle\rangle - \tfrac{1}{3}\bar{\mathbf{I}}\big], \qquad (6a)\end{aligned}$$

where the j subscript is a reminder of the restriction and the outer $\langle\ \rangle$ brackets denote an ensemble average over all thermally distributed initial states. Applying the density operator definition $\rho \equiv \langle|\psi\rangle\langle\psi|\rangle$, the completeness identity $\sum_{j',m'}|j',m'\rangle\langle j',m'| = 1$ (where $j',m' \to j,m$ or J,M), and $\rho_{j'',m'';j',m'} \equiv \langle j'',m''|\rho|j',m'\rangle$, we obtain

$$\begin{aligned}\langle\boldsymbol{\alpha}\rangle_j = \Delta\alpha \sum_{j',m'}\sum_{j'',m''} &\rho_{j'',m'';j',m'}(\mathbf{x},\tau) \\ &\times\left(\langle j',m'|\hat{\mathbf{r}}\hat{\mathbf{r}}|j'',m''\rangle - \frac{1}{3}\bar{\mathbf{I}}\right). \qquad (6b)\end{aligned}$$

The $j'' = j'$ terms $\rho_{j',m'';j',m'}$ have zeroth-order values $\rho^0_{j',m';j',m'}\delta_{m'',m'}$ that are the m'th state's share of the degenerate thermally distributed j'th level populations $\hat{N}_{j'}$ [42]:

$$\hat{n}_{j'} \equiv \rho^0_{j',m';j',m'} = \hat{N}_{j'}/(2j'+1), \quad j' \to j,J, \qquad (7a)$$

$$\hat{N}_{j'} = \frac{\mathfrak{M}_{j'}(2j'+1)}{Z_{j'}}\exp\left[-\frac{hcBj'(j'+1)}{k_BT}\right], \qquad (7b)$$

where $Z_{j'}$ follows from the normalization condition $\sum_{j'}\hat{N}_{j'} = 1$ and $\mathfrak{M}_{j'}$ is the multiplicity determined by the combined atomic and molecular nuclear spins. In nitrogen, $\mathfrak{M}_{j'} = 6$ for even j' and $\mathfrak{M}_{j'} = 3$ for odd j'; in oxygen, $\mathfrak{M}_{j'} = 0$ for even j' and $\mathfrak{M}_{j'} = 1$ for odd j'.

For strongly driven molecules or very low pressures, Raman processes can redistribute the populations of all the molecular $|j',m'\rangle$ states [14,34], including those excluded by the simple two-level model used here. In principle, the model can be generalized to include these redistributions, but it is difficult to carry out because it also requires collisional mixing rates that are not accurately known. Fortunately, these populations remain nearly unperturbed by SRRS processes at atmospheric pressure, the broad bandwidths, and $<10\,\mathrm{J/cm^2}$ fluences found in our collimated beam experiments [10]. This result is confirmed by simple energy balance arguments in the discussions that follow Eqs. (24) and (25). The $j'' = j'$ terms thus satisfy $\rho_{j',m'';j',m'} \simeq \delta_{m'',m'}\hat{n}_{j'}$ and

$$\begin{aligned}&\sum_{j',m',m''}\rho_{j',m'';j',m'}\langle j',m''|\hat{\mathbf{r}}\hat{\mathbf{r}}|j',m'\rangle \\ &\simeq \sum_{j',m'}\hat{n}_{j'}\langle j',m'|\hat{\mathbf{r}}\hat{\mathbf{r}}|j',m'\rangle = \langle\langle\psi^0|\hat{\mathbf{r}}\hat{\mathbf{r}}|\psi^0\rangle\rangle = \frac{1}{3}\bar{\mathbf{I}}, \qquad (8)\end{aligned}$$

which cancels the second term in expression (6b) to give

$$\langle\boldsymbol{\alpha}\rangle_j = \{\boldsymbol{\alpha}\}_j + \{\boldsymbol{\alpha}\}^*_j \qquad (9)$$

where the complex polarizability tensor is

$$\begin{aligned}\{\boldsymbol{\alpha}\}_j &\equiv \sum_{m,M}\rho_{J,M;j,m}(\mathbf{x},\tau)\langle j,m|\boldsymbol{\alpha}|J,M\rangle \\ &= \sum_{m,M}[\rho_{j,m;J,M}(\mathbf{x},\tau)\langle J,M|\boldsymbol{\alpha}|j,m\rangle]^*. \qquad (10)\end{aligned}$$

The time dependence of $\{\boldsymbol{\alpha}\}_j$ follows from the density matrix equations

$$(\partial_\tau + i\omega_j + \gamma_j)\rho_{J,M;j,m}(\mathbf{x},\tau) = \frac{1}{i\hbar}\langle J,M|[V,\rho]|j,m\rangle,$$

where $\gamma_j = \frac{1}{2}\Delta\omega_j$ is the collisional phase relaxation rate, $\Delta\omega_j$ is the corresponding full width at half maximum (FWHM) linewidth, and

$$\begin{aligned}V(\mathbf{x},\tau) &= -\frac{1}{2}\int_{-\pi}^{+\pi}\mathbb{E}(\mathbf{x},t)\cdot\boldsymbol{\alpha}\cdot\mathbb{E}(\mathbf{x},t)\frac{d(\omega_0 t)}{2\pi} \\ &\simeq -\frac{1}{4}\mathbf{E}^*(\mathbf{x},\tau)\cdot\boldsymbol{\alpha}\cdot\mathbf{E}(\mathbf{x},\tau)\end{aligned}$$

is the interaction Hamiltonian, excluding second harmonic terms. (Note that $\mathbf{E}\cdot\boldsymbol{\alpha}\cdot\mathbf{E}^* = \mathbf{E}^*\cdot\boldsymbol{\alpha}\cdot\mathbf{E}$ is real because $\boldsymbol{\alpha} = \boldsymbol{\alpha}^\dagger$.) Again applying the completeness identity and recalling that $\rho_{j',m'';j',m'} \simeq \delta_{m'',m'}\hat{n}_{j'}$, we obtain

$$\begin{aligned}\left(\partial_\tau + i\omega_j + \frac{1}{2}\Delta\omega_j\right)\rho_{J,M;j,m} &= \frac{1}{i\hbar}\sum\nolimits_{m'}(\langle J,M|V|j,m'\rangle\rho_{j,m';j,m} + \langle J,M|V|J,m'\rangle\rho_{J,m';j,m}) \\ &\quad - \frac{1}{i\hbar}\sum\nolimits_{m'}(\rho_{J,M;j,m'}\langle j,m'|V|j,m\rangle + \rho_{J,M;J,m'}\langle J,m'|V|j,m\rangle) \\ &\simeq +i\frac{1}{4}\hbar^{-1}\Delta\hat{n}_j\mathbf{E}^*\cdot\langle J,M|\boldsymbol{\alpha}|j,m\rangle\cdot\mathbf{E} + i\sum\nolimits_{\mu}\left(\delta\omega^{\mu}_{j,m}\rho_{J,M;j,m+\mu} - \delta\omega^{\mu*}_{J,M}\rho_{J,M+\mu;j,m}\right), \qquad (11)\end{aligned}$$

where

$$\Delta\hat{n}_j \equiv \hat{n}_j - \hat{n}_J = \frac{\hat{N}_j}{2j+1} - \frac{\hat{N}_{j+2}}{2j+5} \qquad (12)$$

is the effective population difference and

$$\begin{aligned}\delta\omega^{\mu}_{j',m'} &\equiv \hbar^{-1}\langle j',m'+\mu|V|j',m'\rangle \\ &= -\tfrac{1}{4}\hbar^{-1}\mathbf{E}^*\cdot\langle j',m'+\mu|\boldsymbol{\alpha}|j',m'\rangle\cdot\mathbf{E} \qquad (13)\end{aligned}$$

are generalized ac Stark shifts, which can be complex if $\mu \neq 0$.

We will show below that, at atmospheric pressures and the few hundred $\mathrm{MW/cm^2}$ intensities used in our Nike collimated beam experiments, $|\delta\omega^{\mu}_{j',m'}| \ll \Delta\omega_j$ and can thus be ignored. At intensities $>10\,\mathrm{GW/cm^2}$, they could detune discrete spectral lines, but are not an issue for a continuum spectrum as long as they remain small compared to its width.

Expressions (10) and (11) then reduce to

$$\left(\partial_\tau + i\omega_j + \frac{1}{2}\Delta\omega_j\right)\{\boldsymbol{\alpha}\}_j = \sum_{m,M}\langle j,m|\boldsymbol{\alpha}|J,M\rangle\left(\partial_\tau + i\omega_j + \frac{1}{2}\Delta\omega_j\right)\rho_{J,M;j,m} \simeq \frac{i\Delta\hat{n}_j}{4\hbar}\sum_{m,M}\langle j,m|\boldsymbol{\alpha}|J,M\rangle\mathbf{E}^*\cdot\langle J,M|\boldsymbol{\alpha}|j,m\rangle\cdot\mathbf{E}. \quad (14)$$

Adding and subtracting (14) and its complex conjugate and recalling Eq. (9), we obtain

$$\left(\partial_\tau + \frac{1}{2}\Delta\omega_j\right)\langle\boldsymbol{\alpha}\rangle_j + i\omega_j(\{\boldsymbol{\alpha}\}_j - \{\boldsymbol{\alpha}\}_j^*) = 0, \quad (15a)$$

$$\left(\partial_\tau + \frac{1}{2}\Delta\omega_j\right)(\{\boldsymbol{\alpha}\}_j - \{\boldsymbol{\alpha}\}_j^*) + i\omega_j\langle\boldsymbol{\alpha}\rangle_j = \frac{i\Delta\hat{n}_j}{2\hbar}\sum_{m,M}\langle j,m|\boldsymbol{\alpha}|J,M\rangle\mathbf{E}^*\cdot\langle J,M|\boldsymbol{\alpha}|j,m\rangle\cdot\mathbf{E}. \quad (15b)$$

Applying the operator $(\partial_\tau + \frac{1}{2}\Delta\omega_j)$ to (15a) and substituting the result into (15b), we finally obtain the tensor driven harmonic oscillator equation

$$\left(\partial_\tau^2 + \Delta\omega_j\partial_\tau + \omega_j^2 + \frac{1}{4}\Delta\omega_j^2\right)\langle\boldsymbol{\alpha}\rangle_j = \frac{\omega_j\Delta\hat{n}_j}{2\hbar}\sum_{m,M}\langle j,m|\boldsymbol{\alpha}|J,M\rangle\mathbf{E}^*\cdot\langle J,M|\boldsymbol{\alpha}|j,m\rangle\cdot\mathbf{E}. \quad (16)$$

(At normal atmospheric pressures, $\omega_j^2 + \frac{1}{4}\Delta\omega_j^2 \simeq \omega_j^2$.)

C. Expansion into circularly polarized components

To express the tensor equations (5) (with $\langle\boldsymbol{\alpha}\rangle \to \langle\boldsymbol{\alpha}\rangle_j$) and (16) in a more useful form, we expand all transverse vectors such as $\mathbf{E}$ and $\hat{\mathbf{r}}$ into two opposite circularly polarized components, e.g.,

$$\mathbf{E} = \hat{\boldsymbol{\epsilon}}_{+1}^* E_{+1} + \hat{\boldsymbol{\epsilon}}_{-1}^* E_{-1}, \quad E_{\pm1} = \hat{\boldsymbol{\epsilon}}_{\pm1}\cdot\mathbf{E}, \quad (17)$$

where $\hat{\epsilon}_{\pm1}$ is the transverse part of the orthonormal spherical basis set [43]:

$$\hat{\boldsymbol{\epsilon}}_{+1} \equiv -\frac{\hat{\mathbf{x}} + i\hat{\mathbf{y}}}{\sqrt{2}}, \quad \hat{\boldsymbol{\epsilon}}_{-1} \equiv \frac{\hat{\mathbf{x}} - i\hat{\mathbf{y}}}{\sqrt{2}} = -\hat{\boldsymbol{\epsilon}}_{+1}^*, \quad (18a)$$

$$\hat{\mathbf{x}} = \frac{\hat{\boldsymbol{\epsilon}}_{-1} - \hat{\boldsymbol{\epsilon}}_{+1}}{\sqrt{2}}, \quad \hat{\mathbf{y}} = i\frac{\hat{\boldsymbol{\epsilon}}_{-1} + \hat{\boldsymbol{\epsilon}}_{+1}}{\sqrt{2}}, \quad (18b)$$

where $(\hat{\mathbf{x}}, \hat{\mathbf{y}})$ are the usual transverse unit vectors and $\hat{\boldsymbol{\epsilon}}_0 \equiv \hat{\mathbf{z}}$ lies along the laser propagation direction. These relations satisfy the identities $\hat{\boldsymbol{\epsilon}}_{\pm1}\cdot\hat{\boldsymbol{\epsilon}}_{\pm1}^* = -\hat{\boldsymbol{\epsilon}}_{\pm1}\cdot\hat{\boldsymbol{\epsilon}}_{\mp1} = 1$, $\hat{\boldsymbol{\epsilon}}_{\pm1}\cdot\hat{\boldsymbol{\epsilon}}_{\mp1}^* = -\hat{\boldsymbol{\epsilon}}_{\pm1}\cdot\hat{\boldsymbol{\epsilon}}_{\pm1} = 0$, and $\hat{\boldsymbol{\epsilon}}_{+1}^*\hat{\boldsymbol{\epsilon}}_{+1} + \hat{\boldsymbol{\epsilon}}_{-1}^*\hat{\boldsymbol{\epsilon}}_{-1} = \hat{\mathbf{I}}_\perp$.

Wave equation (5) with $\langle\boldsymbol{\alpha}\rangle \to \langle\boldsymbol{\alpha}\rangle_j$ then expands to

$$\left(\partial_z + \frac{1}{2ik_0}\nabla_\perp^2 + i\frac{1}{2}\beta\partial_\tau^2\right)E_{\pm1}(\mathbf{x},\tau) = iQ_0^j(\mathbf{x},\tau)E_{\pm1}(\mathbf{x},\tau) + iQ_{\pm2}^j(\mathbf{x},\tau)E_{\mp1}(\mathbf{x},\tau), \quad (19)$$

where we define the rotational excitation components

$$Q_0^j(\mathbf{x},\tau) \equiv KN\hat{\boldsymbol{\epsilon}}_{\pm1}\cdot\langle\boldsymbol{\alpha}\rangle_j\cdot\hat{\boldsymbol{\epsilon}}_{\pm1}^* = \left[Q_0^j(\mathbf{x},\tau)\right]^*, \quad (20a)$$

$$Q_{\pm2}^j(\mathbf{x},\tau) \equiv KN\hat{\boldsymbol{\epsilon}}_{\pm1}\cdot\langle\boldsymbol{\alpha}\rangle_j\cdot\hat{\boldsymbol{\epsilon}}_{\mp1}^* = \left[Q_{\mp2}^j(\mathbf{x},\tau)\right]^*, \quad (20b)$$

and $K \equiv 2\pi\omega_0/(n_0c)$. Applying Eq. (A7) of Appendix A and recalling the identities $\hat{\boldsymbol{\epsilon}}_{\pm1}\cdot\hat{\boldsymbol{\epsilon}}_{\pm1}^* = 1$ and $\hat{\boldsymbol{\epsilon}}_{\pm1}\cdot\hat{\boldsymbol{\epsilon}}_{\mp1}^* = 0$, we then expand the driven oscillator equation (16) to

$$\left(\partial_\tau^2 + \Delta\omega_j\partial_\tau + \omega_j^2\right)Q_0^j(\mathbf{x},\tau) = \frac{1}{12}g_j\omega_j\Delta\omega_j\frac{n_0c}{8\pi}|\mathbf{E}(\mathbf{x},\tau)|^2, \quad (21a)$$

$$\left(\partial_\tau^2 + \Delta\omega_j\partial_\tau + \omega_j^2\right)Q_{\pm2}^j(\mathbf{x},\tau) = \frac{1}{2}g_j\omega_j\Delta\omega_j\frac{n_0c}{8\pi}E_{\mp1}^*(\mathbf{x},\tau)E_{\pm1}(\mathbf{x},\tau), \quad (21b)$$

where

$$g_j \equiv \frac{64\pi^4N\Delta\alpha^2}{5n_0^2c\lambda_0h\Delta\omega_j}\frac{(j+1)(j+2)}{2j+3}\Delta\hat{n}_j \quad (22)$$

is the convective steady-state resonant power gain coefficient for opposite polarizations.

We now generalize the formulation to include all the thermally occupied j levels and all diatomic species σ (e.g., $\sigma \equiv$ N_2 and O_2 in air), thus replacing $\langle\boldsymbol{\alpha}\rangle_j \to \langle\boldsymbol{\alpha}\rangle_{\sigma j}$ and generalizing Eqs. (20a) and (20b) to

$$Q_0^{\sigma j}(\mathbf{x},\tau) \equiv KN_\sigma\hat{\boldsymbol{\epsilon}}_{\pm1}\cdot\langle\boldsymbol{\alpha}\rangle_{\sigma j}\cdot\hat{\boldsymbol{\epsilon}}_{\pm1}^* = \left[Q_0^{\sigma j}(\mathbf{x},\tau)\right]^*, \quad (23a)$$

$$Q_{\pm2}^{\sigma j}(\mathbf{x},\tau) \equiv KN_\sigma\hat{\boldsymbol{\epsilon}}_{\pm1}\cdot\langle\boldsymbol{\alpha}\rangle_{\sigma j}\cdot\hat{\boldsymbol{\epsilon}}_{\mp1}^* = \left[Q_{\mp2}^{\sigma j}(\mathbf{x},\tau)\right]^*. \quad (23b)$$

We also sum over the excitation terms in Eq. (19), reinstate the instantaneous electronic nonlinear refractive index n_2^I, and insert a linear attenuation term κ to model O_2 absorption:

$$\left(\partial_z + \frac{1}{2}\kappa + \frac{1}{2ik_0}\nabla_\perp^2 + i\frac{1}{2}\beta\partial_\tau^2\right)E_{\pm1}(\mathbf{x},\tau) = i\left[Q_0(\mathbf{x},\tau) + k_0n_2^I|\mathbf{E}(\mathbf{x},\tau)|^2\right]E_{\pm1}(\mathbf{x},\tau) + iQ_{\pm2}(\mathbf{x},\tau)E_{\mp1}(\mathbf{x},\tau), \quad (24a)$$

$$Q_\mu(\mathbf{x},\tau) \equiv \sum_{\sigma,j}Q_\mu^{\sigma j}(\mathbf{x},\tau), \quad \mu \to 0, \pm2. \quad (24b)$$

Finally, Eqs. (21), (22), and (12) generalize to

$$\left(\partial_\tau^2 + \Delta\omega_{\sigma j}\partial_\tau + \omega_{\sigma j}^2\right)Q_0^{\sigma j}(\mathbf{x},\tau) = \frac{1}{12}\omega_{\sigma j}\Delta\omega_{\sigma j}g_{\sigma j}\frac{n_0c}{8\pi}|\mathbf{E}(\mathbf{x},\tau)|^2, \quad (25a)$$

$$\left(\partial_\tau^2 + \Delta\omega_{\sigma j}\partial_\tau + \omega_{\sigma j}^2\right)Q_{\pm2}^{\sigma j}(\mathbf{x},\tau) = \frac{1}{2}\omega_{\sigma j}\Delta\omega_{\sigma j}g_{\sigma j}\frac{n_0c}{8\pi}E_{\mp1}^*(\mathbf{x},\tau)E_{\pm1}(\mathbf{x},\tau), \quad (25b)$$

$$g_{\sigma j} = \frac{64\pi^4N_\sigma\Delta\alpha_\sigma^2}{5n_0^2c\lambda_0h\Delta\omega_{\sigma j}}\frac{(j+1)(j+2)}{2j+3}\left(\frac{\hat{N}_{\sigma,j}}{2j+1} - \frac{\hat{N}_{\sigma,j+2}}{2j+5}\right). \quad (25c)$$

Expressions (25) are the generalized equivalents of Eq. (4) in Ref. [31] and include not only the Raman Stokes and anti-Stokes frequency shifts, but also other frequency components that account for the Raman-induced noninstantaneous portion of the self-phase modulation. Note that two opposite circular polarizations drive the molecular excitation $Q_{\pm2}^{\sigma j}$ six times harder than $Q_0^{\sigma j}$ from two circular polarizations of the same sign [42].

Equations (24) and (25) provide a physically intuitive SRRS formulation because $E_{\pm1}$ is composed of photon annihilation operators that transfer ±1 units of angular momentum from the light to each molecule, while $E^*_{\pm1}$ is composed of photon creation operators that transfer ±1 units from the molecule back to the light. Excitation $Q_0^{\sigma j}$ thus represents zero net angular momentum transfer $\Delta m = 0$ to the molecules, in agreement with the $|\mathbf{E}|^2$ term in (25a), while excitation $Q_{\pm2}^{\sigma j}$ represents a net angular momentum transfer $\Delta m = \pm2$, in agreement with the $E^*_{\mp1}E_{\pm1}$ term in (25b). In the right-hand side of Eq. (24), the coefficient of the $E_{\pm1}$ term is the $\Delta m = 0$ excitation Q_0, while the coefficient of the $E_{\mp1}$ term must be $Q_{\pm2}$ to provide the $\Delta m = \pm2$ required to drive the opposite circular polarization.

We can now confirm that $g_{\sigma j}$ is indeed the steady-state convective power gain or loss coefficient under the ideal condition where monochromatic beams of opposite circular polarizations interact. To do this, apply Eqs. (24) and (25) to the case where a $+1$ polarized beam E^P_{+1} ($\omega_P = 0$) drives a -1 polarized beam $E^{S/A}_{-}$ ($\omega_{S/A} = \mp\omega_{\sigma j}$), which is either Stokes E^S_- ($\omega_S = -\omega_{\sigma j}$) or anti-Stokes E^A_- ($\omega_A = +\omega_{\sigma j}$), in resonance with the $j \to j+2$ transition of the σth species. Without the attenuation, diffraction, or GVD terms, the relevant part of (24a) reduces to $\partial_z E^{S/A}_{-1} = i(Q^{\sigma j}_{-2})_{\omega_{S/A}} E^P_{+1}$ and the steady-state solution of (25b) reduces to

$$-i\omega_{S/A}\left(Q^{\sigma j}_{-2}\right)_{\omega_{S/A}} = \frac{1}{2}\omega_{\sigma,j} g_{\sigma j}\frac{n_0 c}{8\pi}E^{P*}_{+1}E^{S/A}_{-1},$$

which gives $\partial_z I^{S/A}_{-1} = \pm g_{\sigma j} I^P_{+1} I^{S/A}_{-1}$ for the beam intensities $I_{\pm1} \equiv (n_0 c/8\pi)|E_{\pm1}|^2$.

Using energy balance arguments, we now confirm that the j-level population redistributions remain negligible under the operating conditions of interest. The population difference $\Delta n_{j,m} \equiv \rho_{j,m;j,m} - \rho_{j+2,m-2;j+2,m-2}$ decreases because the SRS process excites weak $j \to j+2$ transitions. Its reduction rate is $\partial_\tau \Delta n_{j,m} = -(\partial_\tau W_j)_M/N\hbar\omega_j$, where $(\partial_\tau W_j)_M$ is the power per unit volume transferred to the molecules when $\hbar\omega_0$ energy pump photons $\propto I^P_{+1}$ convert to $\hbar(\omega_0 - \omega_j)$ energy Stokes photons $\propto I^S_{-1}$; thus $(\partial_\tau W_j)_M = \partial_z I^S_{-1}\omega_j/\omega_0$ and $\partial_\tau \Delta n_{j,m} = -g_{\sigma j} I^P_{+1} I^S_{-1}/N_\sigma \hbar\omega_0$. This assumes only two discrete spectral lines separated by the resonant frequency ν_j, but remains a good approximation when those lines are replaced by narrow spectral channels of width $\Delta\nu_P \approx \Delta\nu_S \approx \Delta\nu_j \ll \nu_j$. Under the operating conditions of interest, however, I^P_{+1} and I^S_{-1} form a continuous spectrum of total width $\Delta\nu_T$ broader than ν_j. Approximately $(\Delta\nu_T - \nu_j)/\Delta\nu_j \sim \Delta\nu_T/\Delta\nu_j$ of these channel pairs contribute to the Raman process, but the intensities I^P_{+1} and I^S_{-1} within each pair would scale down by the factor $\approx \Delta\nu_j/\Delta\nu_T$, thus giving the net scaling $|\partial_\tau \Delta n_{j,m}| \propto \Delta\nu_j/\Delta\nu_T$. Recalling expression (22), we then estimate

$$\frac{|\partial_\tau \Delta n_{j,m}|}{\Delta\hat{n}_j} \sim \frac{32\pi^3\Delta\alpha_\sigma^2}{5h^2c^2\Delta\nu_T}\frac{(j+1)(j+2)}{2j+3}I^P_{+1}I^S_{-1},$$

where $\Delta\hat{n}_j$ is the thermal population difference and $\Delta\alpha_\sigma$ is given in Table I. For a typical bandwidth $\Delta\nu_T \approx 5$ THz, the strong $j = 8 \to 10$ N_2 transition gives $|\partial_\tau \Delta n_{8,m}|/\Delta\hat{n}_j \sim 5 \times 10^5 I^P_{+1} I^S_{-1}$, where the intensities are expressed in GW/cm^2.

TABLE I. Parameters used for the simulations.

Power attenuation coefficient κ	7.5×10^{-6} cm^{-1}
GVD of air at 248.4 nm β	1.2×10^{-6} ps^2/cm
Instantaneous part of n_2	2.6×10^{-10} cm^2/GW
N_2 frequency coefficient B_{N_2}	2.001 cm^{-1}
O_2 frequency coefficient β_{O_2}	1.438 cm^{-1}
N_2 polarizability anisotropy $\Delta\alpha_{N_2}$	1.08×10^{-24} cm^3
O_2 polarizability anisotropy $\Delta\alpha_{O_2}$	1.74×10^{-24} cm^3
Width of transverse window	20 cm
Width of spatial frequency window	6.4 cm^{-1}
Width of temporal window	2500 ps
Incident spectral width (FWHM)	1.1 THz
Frequency window width	26.2 THz

The perturbed population difference integrated over the typical level relaxation and transient buildup times $\approx$100 ps seen in the simulations then satisfies $|\Delta n_{8,m}| < 10^{-3}\Delta\hat{n}_j$ for average intensities of 1 GW/cm^2. Finally, $|\Delta n_{8,m}|$ will be even smaller when other $j \to j+2$ transitions are included because the $j = 8$ level will be partially replenished by the $j = 6 \to 8$ transition and the $j = 10$ level will be partially depleted by the $j = 10 \to 12$ transition.

The Cartesian and circular polarization components are related via Eqs. (17) and (18):

$$E_+ = -\frac{E_x + iE_y}{\sqrt{2}}, \quad E_- = \frac{E_x - iE_y}{\sqrt{2}}, \tag{26a}$$

$$E_x = \frac{E_- - E_+}{\sqrt{2}}, \quad E_y = -i\frac{E_- + E_+}{\sqrt{2}}. \tag{26b}$$

The Cartesian components can be found most easily by applying (26a) to obtain $E_\pm$ at the entrance plane, solving Eqs. (24) and (25), then applying (26b) to recover E_x and E_y at the exit plane. Alternatively, one can use (26a) and (26b) to transform (24) and (25) directly into Cartesian coordinates; (24) then gives (without the nonlinear refraction term)

$$\left(\partial_z + \frac{1}{2}\kappa + \frac{1}{2ik_0}\nabla_\perp^2 + i\frac{1}{2}\beta\partial_\tau^2\right)E_x = i(Q_0 - Q_\parallel)E_x + iQ_\perp E_y, \tag{27a}$$

$$\left(\partial_z + \frac{1}{2}\kappa + \frac{1}{2ik_0}\nabla_\perp^2 + i\frac{1}{2}\beta\partial_\tau^2\right)E_y = i(Q_0 - Q_\parallel)E_y - iQ_\perp E_x, \tag{27b}$$

where

$$Q_\parallel \equiv \frac{Q_{+2} + Q^*_{+2}}{2}, \tag{28a}$$

$$Q_\perp \equiv i\frac{Q_{+2} - Q^*_{+2}}{2}, \tag{28b}$$

and Eqs. (25) give for the corresponding $Q^{\sigma j}_\parallel$ and $Q^{\sigma j}_\perp$ components

$$\left(\partial_\tau^2 + \Delta\omega_{\sigma,j}\partial_\tau + \omega^2_{\sigma,j}\right)Q^{\sigma j}_\parallel = -\frac{1}{4}\omega_{\sigma j}\Delta\omega_{\sigma j}g_{\sigma j}\frac{n_0 c}{8\pi}(|E_x|^2 - |E_y|^2), \tag{29a}$$

$$\left(\partial_\tau^2 + \Delta\omega_{\sigma,j}\partial_\tau + \omega_{\sigma,j}^2\right)Q_\perp^{\sigma j} = +\frac{1}{4}\omega_{\sigma j}\Delta\omega_{\sigma j}g_{\sigma j}\frac{n_0 c}{8\pi}(E_x^* E_y + E_y^* E_x). \quad (29b)$$

These equations are not as transparent as (24) and (25) because Cartesian coordinates are not the natural basis set for describing angular momentum transfers to the molecules, but they do show that depolarization can arise from the main $\Delta m = 2$ terms in linearly polarized incident light E_x if an orthogonally polarized seed beam E_y is also present. If $E_y \to 0$, then Eq. (29b) gives $Q_\perp^{\sigma,j} \to 0$ and (27b) does not allow E_y to grow; hence Eq. (27a) reduces to a scalar equation

$$\left(\partial_z + \frac{1}{2}\kappa + \frac{1}{2ik_0}\nabla_\perp^2 + i\frac{1}{2}\beta\partial_\tau^2\right)E_x = i(Q_0 - Q_\parallel)E_x, \quad (30)$$

which maintains linear polarization. Combining Eqs. (25a) and (29a), we obtain

$$\left(\partial_\tau^2 + \Delta\omega_{\sigma j}\partial_\tau + \omega_{\sigma j}^2\right)\left(Q_0^{\sigma j} - Q_\parallel^{\sigma j}\right) = \frac{1}{2}\omega_{\sigma j}\Delta\omega_{\sigma j}\frac{2}{3}g_{\sigma j}\frac{n_0 c}{8\pi}|E_x|^2, \quad (31)$$

whose steady-state temporal growth rate is 2/3 that of Eq. (25b) for opposite polarizations [42].

Expressions (30) and (31) are equivalent to the equations used in our earlier SRRS simulations [10]. Reference [10] shows that unlike the above example where circularly polarized Stokes and anti-Stokes waves respond independently to a pump beam of opposite circular polarization, these equations predict a Raman SAS coupling term that allows a parasitic redistribution of energy and parametric suppression of exponential growth.

III. SRRS SIMULATION CODE

The computational strategy is similar to that used in Ref. [10]; it first specifies the complete space-time behavior of the incident field $\mathbf{E}(\mathbf{x}_\perp, 0, \tau)$ at the entrance plane $z = 0$, then solves Eqs. (25) and (24) to propagate $\mathbf{E}(\mathbf{x}_\perp, z, \tau)$ to the exit plane z_M, using split-step techniques. Following the same procedure as in Ref. [10], we begin by Fourier transforming Eq. (25) to the ω frequency domain with spectral intensities $(|\mathbf{E}|^2)_\omega$ and $(E_{\mp1}^* E_{\pm1})_\omega$, solving directly for the spectral excitations $\tilde{Q}_0^{\sigma,j}(\omega)$ and $\tilde{Q}_{\pm2}^{\sigma,j}(\omega)$, then transforming back and using (24b) to obtain $Q_0(\mathbf{x}_\perp, 0, \tau)$ and $Q_{\pm2}(\mathbf{x}_\perp, 0, \tau)$. We then substitute these into Eq. (24a) to calculate the fields $E_\pm(\mathbf{x}_\perp, \Delta z, \tau)$ at the first interior grid plane Δz, using a split-step algorithm that effectively lumps the contributions on the right-hand side into thin windows spaced by Δz. This step begins with the exact analytic solutions of the reduced coupled equations

$$\left\{\partial_z - i\left[Q_0(\mathbf{x}_\perp, 0) + k_0 n_2^I |\mathbf{E}(\mathbf{x}_\perp, 0)|^2\right]\right\}E'_{\pm1}(\mathbf{x}_\perp, z) = iQ_{\pm2}(\mathbf{x}_\perp, 0)E'_{\mp1}(\mathbf{x}_\perp, z)$$

to find the intermediate fields $E'_{\pm1}(\mathbf{x}_\perp, \Delta z, \tau)$; the second step includes the propagation terms on the left-hand side of (24a) by Fourier transforming to the $(\mathbf{k}_\perp, \omega)$ frequency domain and applying the linear space-time propagator:

$$\tilde{E}_\pm(\mathbf{k}_\perp, \Delta z, \omega) = \tilde{E}'_\pm(\mathbf{k}_\perp, \Delta z, \omega)\exp\left[(-\kappa - i|\mathbf{k}_\perp|^2/k_0 + i\beta\omega^2)\tfrac{1}{2}\Delta z\right].$$

We then transform back to $E_\pm(\mathbf{x}_\perp, z, \tau)$ and repeat this procedure at each new z plane. In the $\kappa \to 0$ limit, this algorithm conserves energy at each z step.

To model the chaotic ISI input amplitude $\mathbf{E}(\mathbf{x}_\perp, 0, \tau)$, we begin with an (N_x, N_y, N_τ) array of independent Gaussian-distributed complex random numbers of equal rms value, then filter them in the $(\mathbf{k}_\perp, \omega)$ frequency domain using the incident beam's measured spectrum and a Gauss fit to its far-field profile. We then transform to the $(\mathbf{x}_\perp, \tau)$ domain and filter the result using the measured incident pulse shape and apodized near-field profile. In these simulations, we typically choose $N_x = N_y = 64$ or 128 and $N_\tau = 655\,36$ or 131 072. The width of the far-field profile is specified by the FWHM angular width $\Delta\theta = |\Delta\mathbf{k}_\perp|/k_0$ of the ISI field angle spectrum; in these simulations, $\Delta\theta = 8$ or 15 XDL, which corresponds to about 13 or 25 μrad with our 15×15 cm^2 FWHM collimated Nike beams. It is clear from our earlier spectral data that the long tails on the input spectrum can easily self-seed the SRRS process. This, plus the fact that the chaotic ISI light keeps the SRRS process in a perpetual low gain transient regime, eliminates the necessity of including a high divergence random noise source term in our SRRS model [17,20].

Spectral broadening reduces the optical coherence time t_c, which scales as the inverse bandwidth; in these simulations, we estimate t_c by [10]

$$t_c = \int |\tilde{\mathbf{E}}(\nu)|^4 d\nu, \quad \int |\tilde{\mathbf{E}}(\nu)|^2 d\nu \equiv 1,$$

where $|\tilde{\mathbf{E}}(\nu)|^2$ is the normalized spectral intensity. This expression is strictly valid only for purely chaotic light, but it still provides a useful estimate for our SRRS-broadened light. We benchmarked the code for pure linearly polarized light against its earlier version based on the same scalar Eqs. (30) and (31) used in Ref. [10]. The simulations showed excellent agreement, with depolarization effects below numerical noise levels.

IV. ELLIPTICAL VS LINEAR POLARIZATION SIMULATIONS

Table I lists the parameters used in the simulations, which were carried out in three dimensions with 248-nm ISI beams of 8 XDL angular divergence on a 96×96 transverse grid. The incident pulse shape, spectrum, and other parameters are the same as those used in our earlier paper [10], but the transverse grid was reduced from 256×256 and the angular divergence reduced from 30 XDL because of memory limitations. The incident energy was 16.45 J in a flat-top 15-cm square beam and the propagation path was 102 m with 30 planes separated by 3.4 m. Because this algorithm conserves energy, the only net loss is due to the linear attenuation coefficient κ. The simulations compare SRRS broadening capabilities of elliptically polarized vs x-polarized light, where the results agree with those calculated from our scalar formulation described in Ref. [10]. They deal entirely with ISI beams that are temporally and spatially broadband, where the SRRS response never reaches steady state, but remains in a perpetual transient state with lower convective gains.

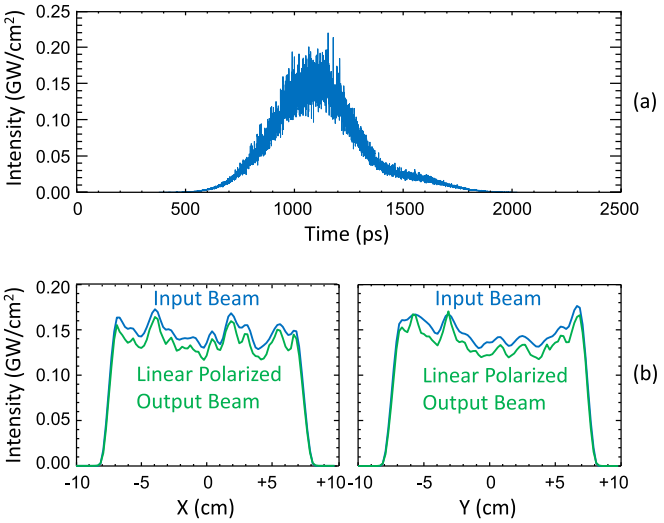

FIG. 2. ISI temporal pulse shapes and spatial profiles. (a) Incident intensity (averaged over the aperture) vs time. (b) Near-field intensity profile lineouts (time averaged over 100 ps around the pulse peak) of x-polarized light at the incident and exit planes, showing finer scale spatial structure and 7.6% linear energy attenuation.

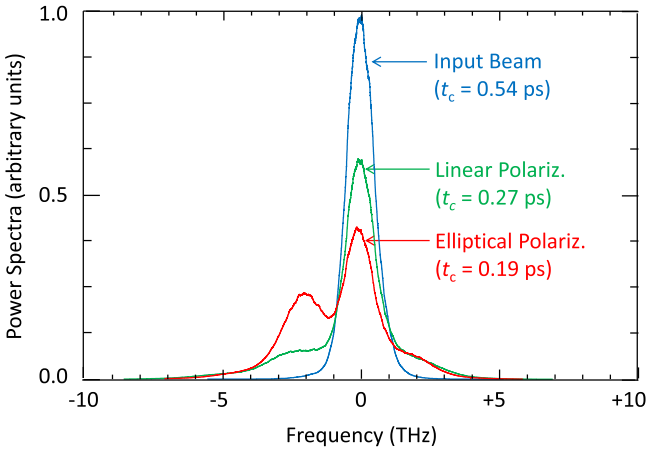

FIG. 3. Comparison of aperture-averaged, time-integrated (and boxcar averaged over 0.1 THz) power spectra at the entrance and exit planes for linear and elliptical polarizations.

Typical ISI temporal pulse shapes and spatial profiles are shown in Fig. 2. Figure 2(a) shows the simulated ISI input ($z = 0$) pulse shapes, which are averaged over the aperture, and Fig. 2(b) compares the near-field intensity profiles of x-polarized light at the incident and exit ($z_M = 102$ m) planes, which are time averaged around the pulse peak. Elliptically polarized light produces similar results. For both polarizations, the pulse shape remains nearly constant along the entire propagation path, except for a ≈7.6% linear attenuation, and the flat-top near-field spatial profiles remain similar at the input and exit planes. The main difference is that the exit plane profiles clearly show the finer structure associated with the higher spatial frequencies due to the SRRS and a small amount of beam walk-off and diffraction around the edges. The nonlinear refractive processes (Raman and electronic) studied here primarily affect the temporal spectra and transverse spatial spectra (i.e., angular divergence and associated far-field broadening).

These simulations show no evidence of the intense near-field filamentation associated with spatially coherent beams [44,45], despite the ≈5-GW average beam power being ≈50 times higher than the ≈100-MW critical power for self-focusing. Unlike the spatially coherent case, the important parameter for ISI light is the effective power within a single coherence zone, whose width is approximately the [aperture width]/XDL; the effective power in our 8 XDL ISI beam is then $(1/8^2) \times 5\,\mathrm{GW} \simeq 80$ MW, which is below the critical power. This filamentation suppression in ISI beams was also predicted by earlier three-dimensional (3D) simulations [46].

Figure 3 compares the aperture-averaged, time-integrated input ($z = 0$) and output ($z = z_M$) power spectra for the case where the input beam polarization is either linear or elliptical with right-hand–left-hand circular components in a 4:1 energy ratio, which was chosen to minimize t_c. The incident spectrum is nearly symmetric with a ≈1.1-THz FWHM bandwidth and calculated coherence time of $t_c = 0.54$ ps. For the linearly polarized case, the output spectrum remains approximately symmetric in its center portion, but exhibits weak sidelobes, especially on the Stokes side; this approximately doubles the effective spectral width and reduces the output coherence time to 0.27 ps. The spreading is primarily due to Raman-induced four-wave mixing, with pump-Stokes conversions creating the small imbalance in favor of the Stokes components. This result is consistent with the parametric suppression mechanism [10,28–30], which is expected for linear polarization; the simulations showed a negligible y-polarized component at the output. For the elliptically polarized case, the output spectrum shows a prominent Stokes-shifted sidelobe corresponding primarily to the N_2 $j = 6 \rightarrow 8$, $8 \rightarrow 10$, and $10 \rightarrow 12$ SRRS transitions; this, in addition to the four-wave mixing process, further reduces the output coherence time to 0.19 ps. These transitions, which are transient with growth times ≈100 ps, are allowed because the opposite but unequal circular components avoid a net linear polarization that would lead to parametric suppression. The average intensity times length integral $\langle I \rangle \times z_M$ is 1490 GW/cm, which is nearly identical to the 1499-GW/cm value calculated in the linearly polarized case.

For the ISI beams modeled here, the broadening occurs in the transverse spatial frequency spectra as well as the temporal spectra. Figure 4 compares lineouts of the input and output transverse spectra, which are averaged over times near the pulse peak, for the case where the input beam polarization is either linear or elliptical. The incident spectrum was modeled by the ISI model described above with an azimuthally symmetric Gaussian envelope of 8 XDL FWHM. For the linearly polarized case, the spectral broadening gives a Strehl ratio ≈0.5, while the elliptically polarized case reduces it to ≈0.25. These spectra are equivalent to the corresponding far-field intensity profiles. Far-field broadening is a potential issue because it can affect beam focusability, but it should be less important for the ≈100 XDL far-field profiles required in laser-fusion applications than for these 8 XDL beams.

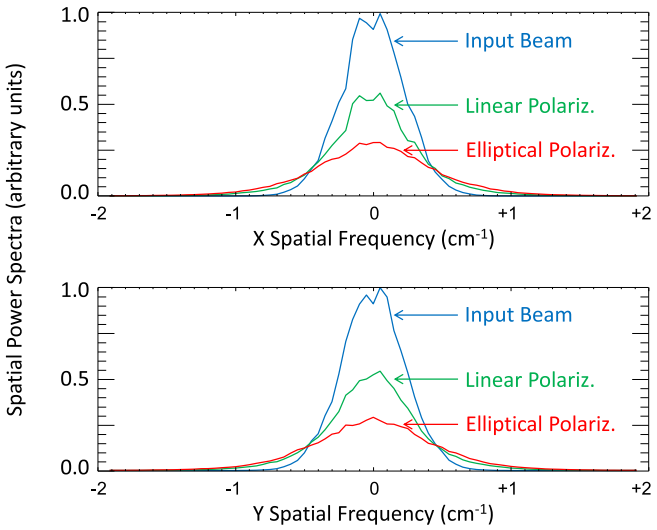

FIG. 4. Comparison of transverse spatial frequency power spectra lineouts (time averaged over 100 ps around the pulse peak) at the input and output for x linear polarization and elliptical polarization.

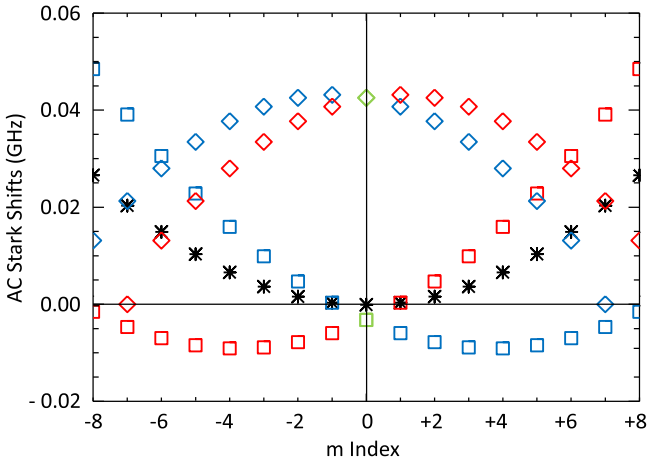

FIG. 5. Stark shifts (in GHz) vs m index of $j = 8$ to $J = 10$ transitions in N_2 at 1 GW/cm^2. Asterisks: $-\delta\nu_0$ for $M = m$, Squares: $-\delta\nu_0$ for $M = m + 2$ (blue), and $M = m - 2$ (red). Diamonds: $|\delta\nu^{\mu}_{j,m}|$ for $\mu = +2$ (blue) and $\mu = -2$ (red).

V. EVALUATION OF THE AC STARK SHIFTS

We now evaluate the ac Stark shifts (13)

$$\delta\omega^{\mu}_{j',m'} = -\tfrac{1}{4}\hbar^{-1}\mathbf{E}^* \cdot \langle j', m' + \mu|\boldsymbol{\alpha}|j', m'\rangle \cdot \mathbf{E} = \delta\omega^{\mu *}_{j',m'} \tag{13}$$

for $j' \to j$ or J, which are nonlinear coefficients of matrix elements such as $\rho_{J,M;j,m+\mu}$ and $\rho_{J,M+\mu;j,m}$ in (11). Unlike the derivation of Eq. (16), one can no longer simplify the treatment by directly summing these terms over m and M because the indices also appear in the matrix elements. Here we focus on $j' \to j$ and just compare the magnitudes of $\delta\omega^{\mu}_{j,m}$ to the oscillator linewidth $\Delta\omega_j$ and resonant frequency ω_j; a more rigorous formulation that fully includes (13) in (11) must be reserved for a later paper. Recalling Eqs. (A5) and (17), we immediately expand the frequency shifts $\delta\nu^{\mu}_{j,m} = \delta\omega^{\mu}_{j,m}/2\pi$ to

$$\delta\nu^{\mu}_{j,m} = \frac{\Delta\alpha}{\sqrt{24}h} C^{j,0}_{j,0;2,0}\big(\delta_{\mu,0}\sqrt{1/6}C^{j,m}_{j,m;2,0}|\mathbf{E}|^2 + \delta_{\mu,+2}C^{j,m+2}_{j,m;2,+2}E^*_{+1}E_{-1} + \delta_{\mu,-2}C^{j,m-2}_{j,m;2,-2}E^*_{-1}E_{+1}\big), \tag{32}$$

where the Clebsch-Gordan coefficients for $\mu \to 0$ and ± 2 are calculated in Appendix B.

For $\mu = 0$, Eq. (B4) gives the usual Stark shift [39]

$$\frac{ch\delta\nu^0_{j,m}}{\Delta\alpha I_{av}} = 10^7\frac{2\pi}{3}\frac{3m^2 - j(j+1)}{(2j+3)(2j-1)}, \tag{33}$$

where I_{av} is in units of W/cm^2. This result was experimentally confirmed by Refs. [40,41]. In Eqs. (11), these terms contribute a net frequency shift $\delta\nu_0(m, M) \equiv \delta\nu^0_{j,m} - \delta\nu^0_{J,M}$, where $J = j + 2$ and M can be m and $m \pm 2$. Figure 5 plots this result for the N_2 $j = 8$ line, using $\Delta\alpha_{N_2} = 1.08 \times 10^{-24}$ cm^3 from Table I and intensity $I_{av} \to 1$ GW/cm^2.

For $\mu = \pm 2$, Eq. (B5) gives

$$\delta\nu^{\pm 2}_{j,m} = -\big|\delta\nu^{\pm 2}_{j,m}\big|_{\max} 2E^*_{\pm 1}E_{\mp 1}/|\mathbf{E}|^2, \tag{34a}$$

where

$$ch\big|\delta\nu^{\pm 2}_{j,m}\big|_{\max}/(\Delta\alpha I_{av}) = 10^7\pi\frac{\sqrt{(j \mp m)(j \mp m - 1)(j \pm m + 2)(j \pm m + 1)}}{(2j+3)(2j-1)}. \tag{34b}$$

These can be regarded as generalized ac Stark shifts, but are actually cross-m transition coefficients. Equation (26a) gives $2E^*_{\pm 1}E_{\mp 1} = |E_y|^2 - |E_x|^2 \pm i(E^*_x E_y + E_x E^*_y)$, whose absolute value satisfies

$$2|E^*_{\pm 1}E_{\mp 1}|/|\mathbf{E}|^2 = \sqrt{|E_y|^4 + |E_x|^4 + E^{*2}_x E^2_y + E^2_x E^{*2}_y}/|\mathbf{E}|^2 \leqslant 1,$$

with $E^*_{\pm 1}E_{\mp 1} \to 0$ for pure circular polarization E_{-1} or $E_{+1} \to 0$. Figure 5 also plots $|\delta\nu^{\pm 2}_{j,m}|_{\max}$ for the N_2 $j = 8$ line, using the same parameters as the $\delta\nu_0(m, M)$ plots, and clearly shows that even at intensities up to 10 GW/cm^2 all of these ac Stark shifts remain negligible compared to the $\Delta\nu_{10,8} \simeq 3$ GHz linewidth.

VI. SUMMARY AND FUTURE WORK

We have generalized the SRRS theory to a full tensor formulation in order to examine the advantages of elliptical polarization over the linearly polarized beams used earlier and to explore the possibility of exploiting the higher SRRS gain allowed by combining mixed circular polarizations. In addition, we performed 3D simulations comparing the spectral broadening capabilities of linear vs elliptical polarizations on low divergence (≈8 XDL) Nike beams. Linear polarization, which limits the SRRS gain by parametric Stokes suppression, produced moderate broadening with little Stokes shift and reduced t_c from 0.54 to 0.27 ps, while elliptical polarization, which avoids that limitation, produced a prominent ≈2-Thz Stokes-shifted sidelobe and reduced t_c to 0.19 ps. This coherence time is still larger than the estimated ≈0.12 ps needed

to suppress CBET and other laser-plasma instabilities, but the path length, pulse shape, and ≈0.15-GW/cm^2 peak envelope intensity used here were chosen only to compare with our earlier results [10]. One can achieve shorter coherence times by just using higher intensities and adjustments in the timing of the two circular polarizations. In addition, the more general formulation presented here will enable us to explore the possibility of combining incident beams of alternating circular polarizations with different spectra and angular divergences to simultaneously reduce both the coherence times and the focal spot broadening.

In future work, we will apply the code to model additional experiments at the Naval Research Laboratory and other facilities with a primary emphasis on how to achieve adequate spectral broadening and short coherence times without excessive far-field broadening and beam quality degradation. Experiments at other facilities include earlier observation of multiple SRRS Stokes orders at the Lawrence Livermore National Laboratory [9] and the ongoing effort to achieve broader bandwidths in the FLUX parametric amplifier system at the University of Rochester Laboratory for Laser Energetics [12].

ACKNOWLEDGMENTS

We acknowledge informative discussions with Jason Bates and John Reintjes at NRL and Norman Kurnit at LLNL. We acknowledge funding by the U.S. Department of Energy (DOE); National Nuclear Security Administration (NNSA).

APPENDIX A

This Appendix expands the tensor equations (5) (with $\langle\boldsymbol{\alpha}\rangle \to \langle\boldsymbol{\alpha}\rangle_j$) and (16) into the two opposite circularly polarized components of the field amplitudes $\mathbf{E}$ using the $\hat{\boldsymbol{\epsilon}}_{\pm1}$ basis defined by expressions (17) and (18). To express the transverse part of the $\boldsymbol{\alpha}$ operator in Eq. (6a) in the $\hat{\boldsymbol{\epsilon}}_{\pm1}$ basis, we first expand it into $\hat{\mathbf{x}}$ and $\hat{\mathbf{y}}$ [39],

$$\begin{aligned}\frac{\boldsymbol{\alpha}}{\Delta\alpha} &= \sum_{\hat{\mathbf{n}}=\hat{\mathbf{x}},\hat{\mathbf{y}}}\sum_{\hat{\mathbf{n}}'=\hat{\mathbf{x}},\hat{\mathbf{y}}} \hat{\mathbf{n}}\hat{\mathbf{n}}\cdot\left(\hat{\mathbf{r}}\hat{\mathbf{r}}-\frac{1}{3}\bar{\mathbf{I}}\right)\cdot\hat{\mathbf{n}}'\hat{\mathbf{n}}' \\ &= \hat{\mathbf{x}}\hat{\mathbf{x}}\left[\frac{1}{2}\sin^2\theta(1+\cos 2\phi)-\frac{1}{3}\right]+\hat{\mathbf{y}}\hat{\mathbf{y}}\left[\frac{1}{2}\sin^2\theta(1-\cos 2\phi)-\frac{1}{3}\right]+(\hat{\mathbf{x}}\hat{\mathbf{y}}+\hat{\mathbf{y}}\hat{\mathbf{x}})\frac{1}{2}\sin^2\theta\sin 2\phi,\end{aligned}$$

then transform $\hat{\mathbf{x}}$ and $\hat{\mathbf{y}}$ to the $\hat{\boldsymbol{\epsilon}}_{\pm1}$ basis to obtain the key quadrupole operator theorem:

$$\begin{aligned}\frac{\boldsymbol{\alpha}}{\Delta\alpha} &= +\frac{1}{2}(\hat{\boldsymbol{\epsilon}}_{-1}-\hat{\boldsymbol{\epsilon}}_{+1})(\hat{\boldsymbol{\epsilon}}_{-1}-\hat{\boldsymbol{\epsilon}}_{+1})\left[\frac{1}{2}\sin^2\theta(1+\cos 2\phi)-\frac{1}{3}\right] \\ &\quad -\frac{1}{2}(\hat{\boldsymbol{\epsilon}}_{-1}+\hat{\boldsymbol{\epsilon}}_{+1})(\hat{\boldsymbol{\epsilon}}_{-1}+\hat{\boldsymbol{\epsilon}}_{+1})\left[\frac{1}{2}\sin^2\theta(1-\cos 2\phi)-\frac{1}{3}\right] \\ &\quad +\frac{i}{4}[(\hat{\boldsymbol{\epsilon}}_{-1}-\hat{\boldsymbol{\epsilon}}_{+1})(\hat{\boldsymbol{\epsilon}}_{-1}+\hat{\boldsymbol{\epsilon}}_{+1})+(\hat{\boldsymbol{\epsilon}}_{-1}+\hat{\boldsymbol{\epsilon}}_{+1})(\hat{\boldsymbol{\epsilon}}_{-1}-\hat{\boldsymbol{\epsilon}}_{+1})]\sin^2\theta\sin 2\phi \\ &= -\sqrt{\frac{8\pi}{15}}\left[\sqrt{\frac{1}{6}}Y_2^0(\theta)\hat{\mathbf{I}}_\perp+Y_2^{+2}(\theta,\phi)\hat{\boldsymbol{\epsilon}}_{+1}^*\hat{\boldsymbol{\epsilon}}_{-1}+Y_2^{-2}(\theta,\phi)\hat{\boldsymbol{\epsilon}}_{-1}^*\hat{\boldsymbol{\epsilon}}_{+1}\right],\end{aligned} \tag{A1}$$

where

$$Y_2^0(\theta)\equiv\sqrt{\frac{5}{16\pi}}(3\cos^2\theta-1), \tag{A2a}$$

$$Y_2^{\pm2}(\theta,\phi)\equiv\sqrt{\frac{15}{32\pi}}\sin^2\theta\exp(\pm 2i\phi) \tag{A2b}$$

are the respective orthonormal $L=2$ spherical harmonic eigenfunctions $|2,0\rangle$ and $|2,\pm2\rangle$. The rotational matrix elements of $Y_L^\mu(\theta,\phi)$ are then real and satisfy the identity [47]

$$\langle j',m'|Y_L^\mu|j,m\rangle=\oint\left(Y_{j'}^{m'}\right)^*Y_L^\mu Y_j^m d\Omega=\sqrt{\frac{(2L+1)(2j+1)}{4\pi(2j'+1)}}C_{j,0;L,0}^{j',0}C_{j,m;L,\mu}^{j',m'}, \tag{A3}$$

where $L\to 2$; $\mu\to 0,\pm2$; and the real matrix elements of interest

$$\begin{aligned}C_{j,m;2,\mu}^{j',m'(=m+\mu)} &\equiv \langle j,m;2,\mu||j',m'\rangle\delta_{m',m+\mu} \\ &= \sqrt{\frac{2j'+1}{2j+1}}C_{j',-m';2,\mu}^{j,-m(=-m'+\mu)}\end{aligned} \tag{A4}$$

are the Clebsch-Gordan (CG) coefficients. Expression (A3) is just the spherical harmonic version of the Wigner-Eckart theorem [47].

To derive the working SRRS equations, substitute these results into (A1):

$$\langle j,m|\frac{\boldsymbol{\alpha}}{\Delta\alpha}|J,M\rangle=-\sqrt{\frac{2(2J+1)}{3(2j+1)}}C^{j,0}_{J,0;2,0}\big(\sqrt{1/6}C^{j,m=M}_{J,M;2,0}\hat{\mathbf{I}}_{\perp}+C^{j,m=M+2}_{J,M;2,+2}\hat{\boldsymbol{\epsilon}}^{*}_{+1}\hat{\boldsymbol{\epsilon}}_{-1}+C^{j,m=M-2}_{J,M;2,-2}\hat{\boldsymbol{\epsilon}}^{*}_{-1}\hat{\boldsymbol{\epsilon}}_{+1}\big),\tag{A5}$$

where $\langle J,M|\boldsymbol{\alpha}/\Delta\alpha|j,m\rangle$ is found by interchanging $j,m\leftrightarrows J,M$. Substituting this into Eq. (16) and applying (17), we obtain

$$\begin{aligned}\frac{\big(\partial_\tau^2+\Delta\omega_j\partial_\tau+\omega_j^2\big)\langle\boldsymbol{\alpha}\rangle_j}{(\Delta\alpha^2/\hbar)\omega_j\Delta\hat{n}_j}&=\sum_{m,M}\langle j,m|\frac{\boldsymbol{\alpha}}{\Delta\alpha}|J,M\rangle\mathbf{E}^{*}\cdot\langle J,M|\frac{\boldsymbol{\alpha}}{\Delta\alpha}|j,m\rangle\cdot\mathbf{E}\\&=\frac{1}{3}C^{j,0}_{J,0;2,0}C^{J,0}_{j,0;2,0}\sum_{m,M}\left(\sqrt{\frac{1}{6}}C^{j,m=M}_{J,M;2,0}\hat{\mathbf{I}}_{\perp}+C^{j,m=M+2}_{J,M;2,+2}\hat{\boldsymbol{\epsilon}}^{*}_{+1}\hat{\boldsymbol{\epsilon}}_{-1}+C^{j,m=M-2}_{J,M;2,-2}\hat{\boldsymbol{\epsilon}}^{*}_{-1}\hat{\boldsymbol{\epsilon}}_{+1}\right)\\&\times\left(\sqrt{\frac{1}{6}}C^{J,M=m}_{j,m;2,0}|\mathbf{E}|^2+C^{J,M=m+2}_{j,m;2,+2}E^{*}_{+1}E_{-1}+C^{J,M=m-2}_{j,m;2,-2}E^{*}_{-1}E_{+1}\right).\end{aligned}\tag{A6}$$

The product of the two brackets gives the terms $C^{j,0}_{J,0;2,0}C^{j,m}_{J,M;2,\nu}C^{J,0}_{j,0;2,0}C^{J,M}_{j,m;2,\mu}$, where μ and ν can be 0 or ±2. Using (A2) and (A3), we can rewrite this as

$$\begin{aligned}C^{j,0}_{J,0;2,0}C^{j,m}_{J,M;2,\nu}C^{J,0}_{j,0;2,0}C^{J,M}_{j,m;2,\mu}&=\frac{4\pi}{5}\langle J,M|Y_2^{-\nu}|j,m\rangle\langle J,M|Y_2^{+\mu}|j,m\rangle=\frac{4\pi}{5}\langle 2,\nu|Y_J^{-M}|j,m\rangle\langle 2,-\mu|Y_J^{-M}|j,m\rangle\\&=\frac{(2j+1)(2J+1)}{5^2}\big(C^{2,0}_{j,0;J,0}\big)^2C^{2,+\nu}_{j,m;J,-M}C^{2,-\mu}_{j,m;J,-M}.\end{aligned}$$

We then combine the completeness identity

$$\sum_{m,M}C^{2,+\nu}_{j,m;J,M}C^{2,-\mu}_{j,m;J,M}=\sum_{m,M}\langle 2,+\nu||j,m;J,M\rangle\langle j,m;J,M||2,-\mu\rangle=\langle 2,+\nu||2,-\mu\rangle=\delta_{\nu,-\mu}$$

with Eq. (B2), which is calculated in Appendix B, to obtain the CG identity

$$\sum_{m,M}C^{j,0}_{J,0;2,0}C^{j,m}_{J,M;2,\nu}C^{J,0}_{j,0;2,0}C^{J,M}_{j,m;2,\mu}=\frac{(2j+1)(2J+1)}{5^2}\big(C^{2,0}_{j,0;J,0}\big)^2\delta_{\nu,-\mu}=\frac{3(j+2)(j+1)}{10(2j+3)}\delta_{\nu,-\mu}.$$

Finally, we apply this identity to (A6) to obtain the driven oscillator equation

$$\big(\partial_\tau^2+\Delta\omega_j\partial_\tau+\omega_j^2\big)\langle\boldsymbol{\alpha}\rangle_j=\frac{(j+1)(j+2)\omega_j\Delta\alpha^2\Delta\hat{n}_j}{10(2j+3)\hbar}\big(|\mathbf{E}|^2\hat{\mathbf{I}}_{\perp}/6+E^{*}_{-1}E_{+1}\hat{\boldsymbol{\epsilon}}^{*}_{+1}\hat{\boldsymbol{\epsilon}}_{-1}+E^{*}_{+1}E_{-1}\hat{\boldsymbol{\epsilon}}^{*}_{-1}\hat{\boldsymbol{\epsilon}}_{+1}\big).\tag{A7}$$

APPENDIX B

This Appendix derives the required Clebsch-Gordan coefficients for $J\to j+2$ or j from the Racah formula [48]:

$$C^{J,m+\mu}_{j,m;2,\mu}=\sqrt{\frac{(2J+1)(J+j-2)!(J-j+2)!(j+2-J)!}{(j+2+J+1)!}}R^{J,m+\mu}_{j,m;2,\mu}S^{J,m+\mu}_{j,m;2,\mu},\tag{B1}$$

where

$$\begin{aligned}R^{J,m+\mu}_{j,m;2,\mu}&\equiv\sqrt{(J+m+\mu)!(J-m-\mu)!(j-m)!(j+m)!(2-\mu)!(2+\mu)!},\\S^{J,m+\mu}_{j,m;2,\mu}&\equiv\sum_k\frac{(-1)^k}{k!(j+2-J-k)!(j-m-k)!(2+\mu-k)!(J-2+m+k)!(J-j-\mu+k)!},\end{aligned}$$

k are integers $\gtrsim0$, and all terms with negative factorials are excluded.

Example 1. Choose $J\to j+2$ and $m=\mu\to0$ to obtain $S^{j+2,0}_{j,0;2,0}=1/(2j!)^2$ and

$$C^{J,0}_{j,0;2,0}\to C^{j+2,0}_{j,0;2,0}=\sqrt{\frac{3(j+2)(j+1)}{2(2j+3)(2j+1)}}.$$

We relate this to $C^{2,0}_{j,0;j+2,0}$ by recalling Eq. (A3) and noting that $\langle J,0|Y_2^0|j,0\rangle=\langle 2,0|Y_J^0|j,0\rangle$:

$$\big(C^{2,0}_{j,0;j+2,0}\big)^2=\frac{5}{2j+5}\big(C^{j+2,0}_{j,0;2,0}\big)^2=\frac{15(j+2)(j+1)}{2(2j+5)(2j+3)(2j+1)}.\tag{B2}$$

Example 2. Choose $J \to j$ and $\mu \to 0$ or ± 2 to obtain

$$S^{j,m+\mu}_{j,m;2,\mu} = \sum_{k=0}^{2} \frac{(-1)^k}{k!(2-k)!(j-m-k)!(2+\mu-k)!(j-2+m+k)!(-\mu+k)!}$$
$$= \frac{6m\mu - 4j - 12jm\mu - 4j^2 + 12m^2 - 2j\mu^2 + 4j^2\mu^2}{2(j-m)!(j+m)!(2+\mu)!(2-\mu)!},$$
$$C^{j,m+\mu}_{j,m;2,\mu} = \sqrt{\frac{(2j+1)(2j-2)!(2)!(2)!}{(2j+3)!}}\sqrt{(j+m+\mu)!(j-m-\mu)!(j-m)!(j+m)!(2-\mu)!(2+\mu)!}S^{j,m+\mu}_{j,m;2,\mu}$$
$$= \sqrt{\frac{(j+m+\mu)!(j-m-\mu)!}{j(2j+3)(j+1)(2j-1)(j-m)!(j+m)!(2+\mu)!(2-\mu)!}}\left[3m\mu - 2j - 6jm\mu - 2j^2 + 6m^2 - j\mu^2 + 2j^2\mu^2\right],$$

which reduces to

$$C^{j,0}_{j,0;2,0} = -\sqrt{\frac{j(j+1)}{(2j+3)(2j-1)}}.$$

These combine to give

$$C^{j,0}_{j,0;2,0}C^{j,m+\mu}_{j,m;2,\mu} = -\sqrt{\frac{(j+m+\mu)!(j-m-\mu)!}{(j-m)!(j+m)!(2+\mu)!(2-\mu)!}}\frac{3m\mu - 2j - 6jm\mu - 2j^2 + 6m^2 - j\mu^2 + 2j^2\mu^2}{(2j+3)(2j-1)}. \tag{B3}$$

For $\mu \to 0$ and ± 2, Eq. (32) then gives

$$-\delta\nu^0_{j,m} = \frac{\Delta\alpha}{6h}\frac{3m^2 - j(j+1)}{(2j+3)(2j-1)}|\mathbf{E}|^2, \tag{B4}$$

$$-\delta\nu^{\pm 2}_{j,m} = \frac{\Delta\alpha}{2h}\frac{\sqrt{(j\mp m)(j\mp m-1)(j\pm m+2)(j\pm m+1)}}{(2j+3)(2j-1)}E^*_{\pm 1}E_{\mp 1}. \tag{B5}$$

[1] D. Eimerl, W. L. Kruer, and E. M. Campbell, Ultrabroad bandwidth for suppression of laser driven parametric instabilities, Comments Plasma Phys. **15**, 85 (1992).

[2] C. J. Randall, J. R. Albritton, and J. J. Thomson, Theory and simulation of stimulated Brillouin scatter excited by nonabsorbed light in laser fusion systems, Phys. Fluids **24**, 1474 (1981).

[3] W. L. Kruer, *The Physics of Laser Plasma Interactions* (Westview, Boulder, 2003).

[4] J. W. Bates, R. K. Follett, J. G. Shaw, S. P. Obenschain, R. H. Lehmberg, J. F. Myatt, J. L. Weaver, D. M. Kehne, M. F. Wolford, M. C. Myers, and T. J. Kessler, Suppressing cross-beam energy transfer with broadband lasers, High Energy Density Phys. **36**, 100772 (2020), and references therein.

[5] R. K. Follett, J. G. Shaw, J. F. Myatt, J. P. Palastro, R. W. Short, and D. H. Froula, Suppressing Two-Plasmon Decay with Laser Frequency Detuning, Phys. Rev. Lett. **120**, 135005 (2018).

[6] Y. Zhao, S. Weng, M. Chen, J. Zheng, H. Zhuo, and Z. Sheng, Stimulated Raman scattering excited by incoherent light in plasma, Matter Radiat. Extremes **2**, 190 (2017).

[7] The intrinsic bandwidth of NIF is limited to ≈ 0.27 THz, OMEGA can provide up to 1 THz, and the Nike KrF laser has demonstrated up to 3 THz.

[8] M. F. Wolford, M. C. Myers, Tz. B. Petrova, J. L. Giuliani, T. J. Kessler, M. W. McGeoch, G. M. Petrov, A. J. Schmitt, T. A. Mehlhorn, and S. P. Obenschain, Development of a broad bandwidth 193 nanometer laser driver for inertial confinement fusion, High Energy Density Phys. **36**, 100801 (2020).

[9] D. Eimerl, D. Milam, and J. Yu, Large bandwidth Frequency-Converted Nd:Glass Laser at 527 nm with $\Delta v/v = 2\%$, Phys. Rev. Lett. **70**, 2738 (1993).

[10] J. Weaver, R. Lehmberg, S. Obenschain, D. Kehne, and M. Wolford, Spectral and far-field broadening due to stimulated Raman scattering driven by the Nike krypton fluoride laser, Appl. Opt. **56**, 8618 (2017).

[11] Z. Epstein, R. H. Lehmberg, and P. Sprangle, Spectral broadening of a KrF laser via propagation through Xe in the negative nonlinear index regime, Phys. Rev. A **100**, 023831 (2019)

[12] C. Dorrer, E. M. Hill, and J. D. Zuegel, High-energy parametric amplification of spectrally incoherent broadband pulses, Opt. Express **28**, 451 (2020).

[13] N. Bloembergen, *Nonlinear Optics* (Addison-Wesley, Reading, MA, 1992).

[14] W. Kaiser and M. Maier, Stimulated Rayleigh, Brillouin and Raman spectroscopy, in *Laser Handbook* (North-Holland, Amsterdam, 1972).

[15] M. A. Henesian, C. D. Swift, and J. R. Murray, Stimulated rotational Raman scattering in nitrogen in long air paths, Opt. Lett. **10**, 565 (1985).

[16] N. A. Kurnit, Calculation and measurement of stimulated rotational Raman scattering in atmospheric oxygen, Los Alamos National Laboratory Report No. LA-UR-4145 (1995).

[17] Y. Lin, T. J. Kessler, and G. N. Lawrence, Raman scattering in air: Four-dimensional analysis, Appl. Opt. **33**, 4781 (1995).

[18] M. D. Skeldon and R. Bahr, Stimulated rotational Raman scattering in air with a high power broadband laser, Opt. Lett. **16**, 366 (1991).

[19] Xin-Min Fan, Zhi-Wei Lü, Dian-Yang Lin, Ying Liu, Cheng-Yu Zhu, Wei-Ming He, and Lei Ding, Investigation of stimulated rotational Raman scattering of the high power broadband laser with applied angular dispersion, Chin. Phys. B **22**, 124206 (2013).

[20] C. Y. Zhu *et al.*, The modified SRRS threshold criteria for high peak power laser pulses in long air-path transmission considering the near-field beam quality, Appl. Phys. B **122**, 272 (2016).

[21] X. M. Fan *et al.*, Numerical investigation of the effects of smoothing by spectral dispersion on stimulated rotational Raman scattering, Laser Part. Beams **31**, 171 (2013).

[22] B. M. Van Wonterghem *et al.*, Operations on the national ignition facility, Fusion Sci. Technol. **69**, 452 (2016).

[23] Obenschain, R. Lehmberg, D. Kehne, F. Hegeler, M. Wolford, J. Sethian, J. Weaver, and M. Karasik, High energy krypton fluoride lasers for inertial fusion, Appl. Opt. **54**, F103 (2015)

[24] R. H. Lehmberg and S. Obenschain, Use of induced spatial incoherence for uniform illumination of laser fusion-targets, Opt. Commun. **46**, 27 (1983).

[25] R. H. Lehmberg and J. Goldhar, Use of incoherence to produce smooth and controllable irradiation profiles with KrF fusion lasers, Fusion Technol. **11**, 532 (1987).

[26] J. M. D. Lister, M. J. Shaw, C. J. Hooker, and E. C. Harvey, Uniform target illumination by induced spatial incoherence in a multiplexed KrF laser system, Opt. Commun. **84**, 55 (1991).

[27] X. Yi-Huai, G. Zhi-Xing, T. Xiao-Hui, D. Hui, T. Xiu-Zhang, and S. Yu-Sheng, Beam smoothing investigation on Heaven I, Proc. SPIE **6279**, 62795Z (2007).

[28] M. D. Duncan, R. Mahon, J. Reintjes, and L. L. Tankersley, Parametric Raman gain suppression in D2 and H2, Opt. Lett. **11**, 803 (1986).

[29] M. A. Henesian and D. M. Pennington, Observation of parametric gain suppression in stimulated rotational Raman scattering over long air paths, Paper No. WN1, in Proceedings of the Conference on Lasers and Electro-Optics, 1986 (unpublished).

[30] K. Leung, M. Oron, D. Klemek, R. Holmes, and A. Flusberg, Observation of parametric gain suppression in rotational Raman transitions of N2 and H2, Opt. Lett. **13**, 33 (1988).

[31] J. P. Palastro, Time-dependent polarization states of high power, ultrashort laser pulses during atmospheric propagation, Phys. Rev. A. **89**, 013804 (2014), and private communication.

[32] J. R. Penano, P. Sprangle, P. Serafim, B. Hafizi, and A. Ting, Stimulated Raman scattering of intense laser pulses in air, Phys. Rev. E **68**, 056502 (2003).

[33] A. P. Hickman, J. A. Paisner, and W. K. Bischel, Theory of multiwave propagation and frequency conversion in a Raman medium, Phys. Rev. A **33**, 1788 (1986).

[34] C. G. Parazzoli, C. Drutman, and D. M. Capps, Semiclassical theory and numerical modeling for stimulated rotational Raman scattering in homonuclear diatomic molecules, IEEE J. Quantum Electron. **QE26**, 744 (1990).

[35] Yu. A. Il'inskii and V. D. Taranukhin, Polarization characteristics of resonance Raman and hyper-Raman scattering of light in gases, Sov. J. Quant. Electron. **5**, 944 (1976).

[36] R. Boyd, *Nonlinear Optics* (Academic, New York, 2008).

[37] R. Holmes and A. Flusberg, Rotationally invariant theory of stimulated Raman scattering, Phys. Rev. A **37**, 1588 (1988).

[38] S. Zahedpour, J. K. Wahlstrand, and H. M. Milchberg, Measurement of the nonlinear refractive index of air constituents at mid-infrared wavelengths, Opt. Lett. **40**, 5794 (2015).

[39] W. H. Flygare, *Molecular Structure and Dynamics* (Prentice-Hall, Englewood Cliffs, NJ, 1978).

[40] M. E. Mack, R. L. Carman, J. Reintjes, and N. Blömbergen, Transient stimulated rotational and vibrational Raman scattering in gases, Appl. Phys. Lett. **16**, 209 (1970).

[41] R. L. Farrow and L. A. Rahn, Optical stark splitting of rotational Raman transitions, Phys. Rev. Lett. **48**, 395 (1982).

[42] M. Rokni and A. Flusberg, Stimulated rotational Raman scattering in the atmosphere, IEEE J. Quantum Electron. **QE-22**, 1102 (1986); the discussion of the O_2 triplet in Eq. (9) of this reference is clarified by N. A. Kurnit, Calculation and measurement of stimulated rotational Raman scattering in atmospheric oxygen, Paper No. CThK57, in Proceedings of the Conference on Lasers and Electro-Optics, 1996 (unpublished) [OSA Technical Digest **9**, 434 (1996)].

[43] I. Sobel'man, *Introduction to the Theory of Atomic Spectra* (Pergamon, New York, 1962).

[44] I. V. Smetanin, A. O. Levchenko, A. V. Shutov, N. N. Ustinovskii, and V. D. Zvorykin, Role of coherent resonant nonlinear processes in the ultrashort KrF laser pulse propagation and filamentation in air, Nucl. Instrum. Methods Phys. Res. Sect. B **369**, 87 (2016).

[45] V. D. Zvorykin *et al.*, Experimental capabilities of the GARPUN-MTW Ti:sapphire KrF laser facility for investigating the interaction of subpicosecond UV pulses with targets, Quantum Electron. **47**, 319 (2017).

[46] A. J. Schmitt, Three-dimensional filamentation of light in laser plasmas, Phys. Fluids **B3**, 186 (1991).

[47] E. Merzbacher, *Quantum Mechanics* (Wiley, New York, 1961), Chap. 22.

[48] A. Bohm and M. Loewe, *Quantum Mechanics: Foundations and Applications*, 3rd ed. (Springer, New York, 1993).